

Absorption and scattering limits of silicon nitride integrated photonics in the visible spectrum: supplement

MATEUS CORATO-ZANARELLA,^{1,4}  XINGCHEN JI,^{1,2}  ASEEMA MOHANTY,^{1,3}  AND MICHAL LIPSON^{1,5}

¹*Department of Electrical Engineering, Columbia University, New York, New York 10027, USA*

²*John Hopcroft Center for Computer Science, Shanghai Jiao Tong University, Shanghai 200240, China*

³*Department of Electrical and Computer Engineering, Tufts University, Medford, MA 02155, USA*

⁴*mcz2109@columbia.edu*

⁵*ml3745@columbia.edu*

This supplement published with Optica Publishing Group on 2 February 2024 by The Authors under the terms of the [Creative Commons Attribution 4.0 License](#) in the format provided by the authors and unedited. Further distribution of this work must maintain attribution to the author(s) and the published article's title, journal citation, and DOI.

Supplement DOI: <https://doi.org/10.6084/m9.figshare.24680985>

Parent Article DOI: <https://doi.org/10.1364/OE.505892>

Absorption and scattering limits of silicon nitride integrated photonics in the visible spectrum: supplement

MATEUS CORATO-ZANARELLA^{1,*}, XINGCHEN JI^{1,2}, ASEEMA MOHANTY^{1,3}, AND MICHAL LIPSON^{1,*}

¹*Department of Electrical Engineering, Columbia University, New York, New York 10027, USA*

²*John Hopcroft Center for Computer Science, Shanghai Jiao Tong University, Shanghai 200240, China*

³*Department of Electrical and Computer Engineering, Tufts University, Medford, MA 02155, USA*

*Corresponding author: mc22109@columbia.edu (M.C.Z.); ml3745@columbia.edu (M.L.)

1. LOSS MEASUREMENT TECHNIQUES

In the following subsections we present a brief overview of popular loss measurement techniques, highlighting their shortcomings in extracting the absorption and scattering losses of integrated waveguides based on thin films.

A. Ellipsometry

Ellipsometry [1, 2] is a conventional method for measuring refractive index (n), extinction coefficient (k) and thickness of films. However, its sensitivity for the optical constants n and k scales with the optical length of the sample (thickness times refractive index), limiting its effectiveness for thin films. For a thickness on the order of 1000 Å, for example, a change of a few angstroms has the same effect on the optical length as a change in the low third decimal place of the refractive index. In terms of propagation loss, a k sensitivity of on the third decimal place corresponds to an uncertainty on the order of thousand dB/cm. Consequently, ellipsometry alone cannot determine the true transparency window of a thin film. Furthermore, ellipsometry cannot measure scattering losses, which are ubiquitous in photonics integrated circuits.

B. Cutback and outscattered light

Cutback [3–7] is one of the most popular loss measurement techniques for integrated circuits, as it does not require narrow linewidth or tunable laser sources. By comparing the output power of waveguides with different lengths, it provides the loss per unit length. However, it is very susceptible to variations in the coupling loss among the different waveguides, limiting its sensitivity. An alternative method that requires only one waveguide is the measurement of its outscattered light [6, 7]. By fitting the intensity decay as a function of the propagation length, one can extract the loss per unit length. However, neither method can discriminate absorption and scattering, and they both require prohibitively long waveguides to measure ultra-low losses.

C. Photothermal spectroscopy

Photothermal spectroscopy [8–14] uses the light absorption-induced thermal response of a material to measure its optical absorption coefficient. Despite being highly sensitive in principle, this technique relies on the knowledge of a number of material and geometrical properties, making it unsuitable for characterizing arbitrary materials in arbitrary spectral ranges. This is particularly true for deposited amorphous films, whose properties are subject to uncertainty due to their strong dependence on the deposition conditions [15–19]. In addition, this technique cannot measure scattering losses.

2. OPTICAL, STRUCTURAL AND COMPOSITIONAL CHARACTERIZATION OF THE FILMS

In Fig. 1a of the main text, the ellipsometry data was measured by J.A. Woollam Company, and the compositional data was measured via Energy Dispersive X-Ray Spectroscopy (EDS) by Covalent Metrology Services.

Fig. S1 shows the EDS and the Transmission Electron Microscopy (TEM) analysis of the two silicon nitride (SiN) films. The high-magnification TEM images in Fig. S1b highlight the amorphous and dense structure of the films, with no visible volumetric defects. Tables S1 and S2 summarize the EDS compositional analysis of the areas in Fig. S1c, which shows homogeneous distribution of nitrogen and silicon across the films. The lamellas were prepared on a Thermo-Fisher(FEI) Helios UC FIB-SEM system. The TEM images were measured on a Thermo-Fisher(FEI) Talos with bright XFEG source, and the EDS data was measured on a Thermo-Fisher system. The EDS and TEM measurements were performed by Covalent Metrology Services.

Table S1. Atomic composition of the SiN film with Si/N = 0.82 over the area shown in Figure S1c (left panel).

Element	Atomic fraction (%)	Atomic Error (%)	Mass Fraction (%)	Mass Error (%)	Fit Error (%)
N	52.92	9.78	36.61	4.26	0.76
O	3.22	0.88	2.55	0.59	0.5
Al	0.29	0.08	0.39	0.09	0.93
Si	43.48	11.6	60.31	13.56	0.06
Cl	0.08	0.02	0.14	0.03	0.45

Table S2. Atomic composition of the SiN film with Si/N = 0.91 over the area shown in Fig. S1c (right panel).

Element	Atomic fraction (%)	Atomic Error (%)	Mass Fraction (%)	Mass Error (%)	Fit Error (%)
N	50.76	9.77	34.52	4.17	0.08
O	2.84	0.79	2.2	0.51	0.29
Al	0.33	0.09	0.43	0.1	1.2
Si	45.98	12.52	62.7	14.25	0.69
Cl	0.09	0.02	0.16	0.03	0.34

3. MICRORING RESONANCE FITTING AND INTRINSIC LOSS EXTRACTION

We employ temporal coupled mode theory to model the microring resonators [20] and to extract their intrinsic losses from the measured resonances.

The power transmission \mathcal{T} of a microring resonator around a resonant angular frequency ω_0 is typically characterized by a Lorentzian dip of the form [20]

$$\mathcal{T}(\omega) = \frac{|j2(\omega - \omega_0)/\omega_0 + 1/Q_i - 1/Q_c|^2}{|j2(\omega - \omega_0)/\omega_0 + 1/Q_i + 1/Q_c|^2} \quad (\text{S1})$$

where ω is the angular frequency of the light, Q_i is the intrinsic quality factor (Q), and Q_c is the Q corresponding to the coupling rate between the bus waveguide and the microresonator. Examples of such resonances can be seen in Figs. 1b, 3b, and the four leftmost panels of 4b in the main text.

In addition to causing surface scattering that lowers Q_i , random surface roughness on the waveguide walls can also result in intrinsic backscattering. In this case, the propagating clockwise (CW) mode couples to the counter-clockwise (CCW) mode, generating standing-wave patterns. The microring transmission in this case is given by [20]

$$\mathcal{T}(\omega) = \left| 1 - \frac{[j4(\omega - \omega_0)/\omega_0 + 1/\bar{Q}_+ + 1/\bar{Q}_-]/Q_c}{[j2(\omega - \omega_0)/\omega_0 - 1/Q_{split} + 1/\bar{Q}_+][j2(\omega - \omega_0)/\omega_0 + 1/Q_{split} + 1/\bar{Q}_-]} \right|^2 \quad (\text{S2})$$

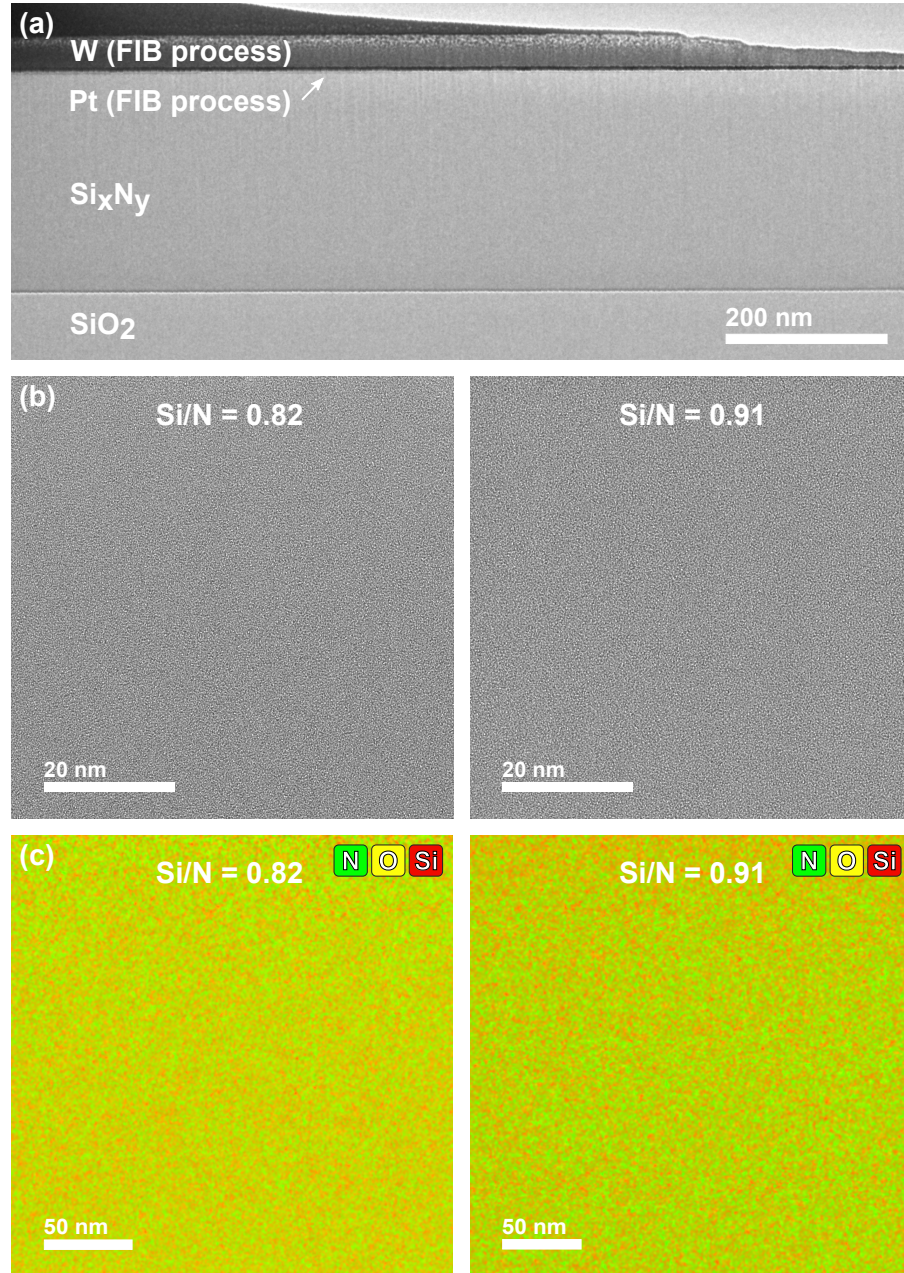


Fig. S1. Energy Dispersive X-Ray Spectroscopy (EDS) and Transmission Electron Microscopy (TEM) analysis of the SiN films. (a) Large-area TEM image of the as-deposited SiN film ($\text{Si}/\text{N} = 0.82$) on top of thermally-grown silicon dioxide (SiO_2). The tungsten (W) and platinum (Pt) thin films were deposited on top for the focused ion beam (FIB) lamella preparation. (b) High-magnification TEM images of the two SiN films, showing their amorphous and dense nature without visible volumetric defects. (c) EDS atomic fraction map of the two SiN films, showing their nitrogen (N), oxygen (O) and silicon (Si) content. The O fraction is much smaller than N and Si (Tables S1 and S2), which are distributed homogeneously across the films.

where Q_{split} is the Q related to the backscattering strength, and $1/\bar{Q}_{\pm} = 1/Q_{i\pm} + 1/Q_c$, with $Q_{i\pm}$ corresponding to the intrinsic Qs of the standing-wave modes. In general, Q_{i+} and Q_{i-} can differ slightly due to the distinct energy distributions of the standing waves. Although intrinsic backscattering is always present [21, 22], it is typically too weak ($Q_{\text{split}} \geq \sqrt{3}\bar{Q}$) to cause an appreciable change in the microresonator transmission, which remains a singlet. However, if the linewidth is small enough compared to the backscattering strength ($Q_{\text{split}} < \sqrt{3}\bar{Q}$), the transmission turns into a split doublet, as seen in the rightmost panel of Fig. 4b in the main text [20].

For all our measurements, the microresonators are undercoupled, implying $Q_i < Q_c$. We use this condition in conjunction with Eqs. (S1) and (S2) to fit the measured resonances and uniquely determine Q_i (or $Q_{i\pm}$). For doublets, we use Eq. (S2), and select Q_i as the highest of Q_{i+} and Q_{i-} to best represent the intrinsic losses of the resonator. For singlets, we use Eq. (S1). In this case, even though some weak intrinsic backscattering might be present and causing a slight linewidth broadening, the absence of a doublet makes it unfeasible to determine Q_{split} confidently. Such uncertainty would introduce appreciable errors in the fitted $Q_{i\pm}$ and Q_c . Therefore, by using Eq. (S1), we conservatively determine a lower bound for Q_i .

From Q_i , we obtain the intrinsic power loss coefficient α via [20]

$$\alpha = \frac{2\pi n_g}{Q_i \lambda_0} \quad (\text{S3})$$

where λ_0 is the resonant wavelength, and n_g is the group index of the mode obtained from a Finite Difference Eigenmode (FDE) solver that employs the refractive indices of the materials measured via ellipsometry.

Since the point coupling scheme may excite higher order modes in the wider waveguides that are not single-mode, we identify the fundamental mode for each polarization as the one with the lowest loss and by its free spectral range (FSR). This is possible because higher order modes present higher loss due to their increased overlap with the sidewalls, and different FSRs due to their different group indices.

In our measurements, most resonances did not show doublets. However, with a dataset of enough split resonances, one could envision extracting the backscattering strength from the fitted Q_{split} as a function of wavelength and waveguide geometry. This would allow one to verify the validity of the model presented in [21, 22] for the distributed backscattering induced by surface roughness.

4. MEASURED PROPAGATION LOSSES ACROSS THE VISIBLE SPECTRUM

Fig. S2 shows the measured propagation losses (α) and intrinsic quality factors (Q_i) of all the microresonator geometries as a function of the sidewall overlap coefficient η_{sides} for the wavelengths around 780 nm, 644 nm, 532 nm, and 461 nm. The coefficient η_{sides} is defined in Eq. (2) of the main text and in Eq. (S12) of section 5A. The Tables S3 to S12 show the datasets that support Fig. 2b of the main text and Fig. S2.

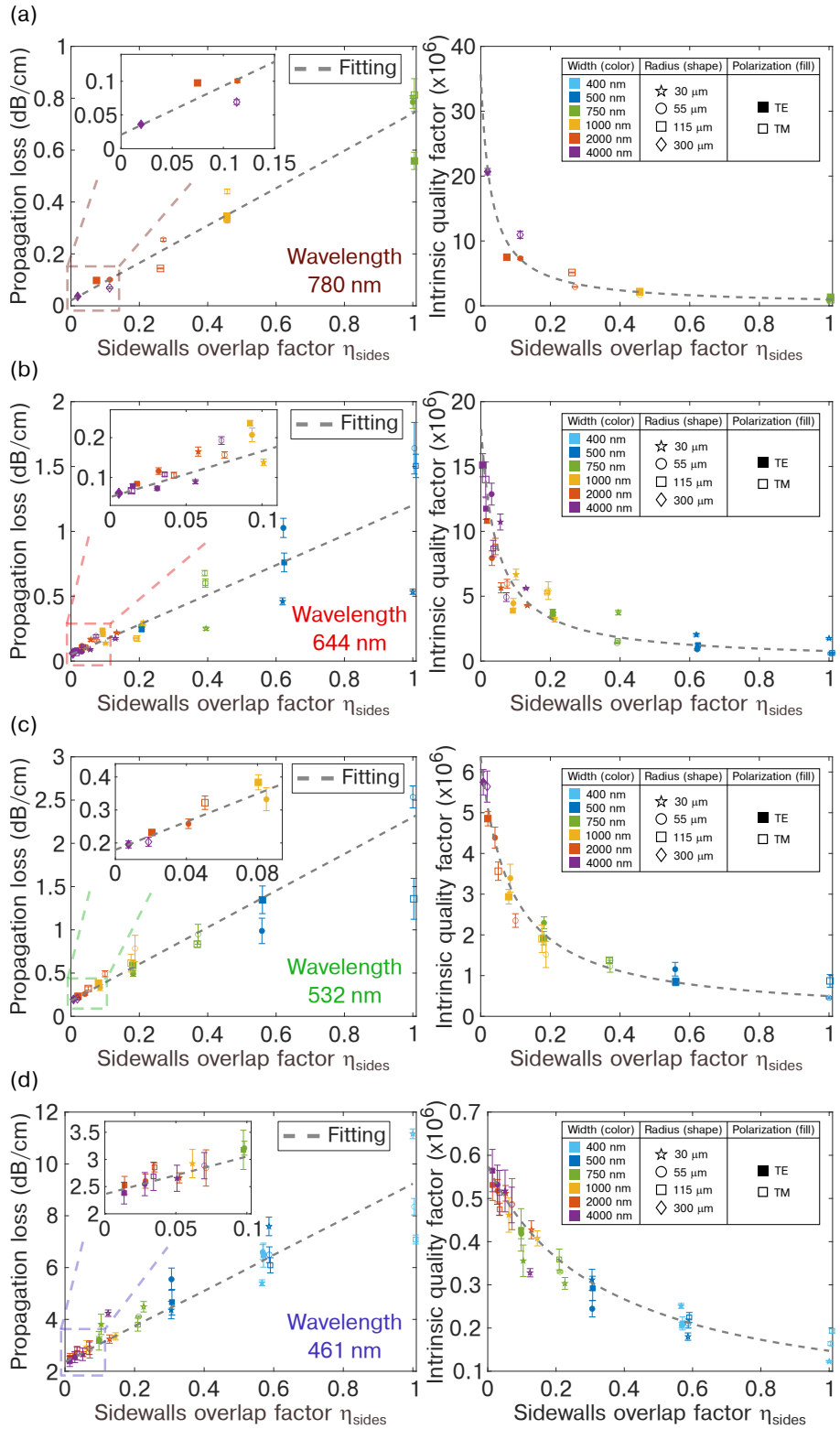


Fig. S2. Measured propagation losses (left) and intrinsic quality factors (right) as a function of the sidewalls overlap factor ($\eta_{\text{sid}} = \frac{\text{width}}{\text{radius}}$) across different spectral regions. (a) 780 nm wavelength. (b) 644 nm wavelength. (c) 532 nm wavelength. (d) 461 nm wavelength. The dataset for 488 nm wavelength is depicted in Fig. 2 of the main text. The errorbars correspond to the mean \pm s.d. of tens of consecutive measurements for all the recorded laser detunings of each resonance (e.g. Fig. 3b, top of the main text).

Table S3. Measured intrinsic quality factors and propagation losses for the fundamental TE mode of microresonators with varying cross-sections at 780 nm wavelength. For each pair of width and radius, the first row is the intrinsic quality factor, and the second is the propagation loss.

Width (nm) \ Radius (μm)	55	115	300
750	$(9.5 \pm 0.3) \times 10^5$ (0.79 ± 0.02) dB/cm	$(1.33 \pm 0.08) \times 10^6$ (0.56 ± 0.03) dB/cm	N/A
1000	$(2.25 \pm 0.05) \times 10^6$ (0.328 ± 0.008) dB/cm	$(2.13 \pm 0.06) \times 10^6$ (0.35 ± 0.01) dB/cm	N/A
2000	$(7.3 \pm 0.2) \times 10^6$ (0.101 ± 0.003) dB/cm	$(7.5 \pm 0.2) \times 10^6$ (0.098 ± 0.003) dB/cm	N/A
4000	N/A	N/A	$(2.07 \pm 0.05) \times 10^7$ (0.0362 ± 0.0008) dB/cm

Table S4. Measured intrinsic quality factors and propagation losses for the fundamental TM mode of microresonators with varying cross-sections at 780 nm wavelength. For each pair of width and radius, the first row is the intrinsic quality factor, and the second is the propagation loss.

Width (nm) \ Radius (μm)	55	115	300
750	$(9.23 \pm 0.06) \times 10^5$ (0.805 ± 0.005) dB/cm	$(9.2 \pm 0.7) \times 10^5$ (0.81 ± 0.06) dB/cm	N/A
1000	$(1.68 \pm 0.03) \times 10^6$ (0.441 ± 0.009) dB/cm	$(2.20 \pm 0.03) \times 10^6$ (0.337 ± 0.004) dB/cm	N/A
2000	$(2.92 \pm 0.07) \times 10^6$ (0.255 ± 0.006) dB/cm	$(5.14 \pm 0.06) \times 10^6$ (0.144 ± 0.002) dB/cm	N/A
4000	N/A	N/A	$(1.10 \pm 0.06) \times 10^7$ (0.069 ± 0.004) dB/cm

Table S5. Measured intrinsic quality factors and propagation losses for the fundamental TE mode of microresonators with varying cross-sections at 644 nm wavelength. For each pair of width and radius, the first row is the intrinsic quality factor, and the second is the propagation loss.

Width (nm) \ Radius (μm)	30	55	115	300
500	$(2.0 \pm 0.1) \times 10^6$ (0.46 ± 0.03) dB/cm	$(9.1 \pm 0.6) \times 10^5$ (1.03 ± 0.07) dB/cm	$(1.2 \pm 0.1) \times 10^6$ (0.76 ± 0.07) dB/cm	N/A
750	$(3.6 \pm 0.2) \times 10^6$ (0.25 ± 0.01) dB/cm	$(3.4 \pm 0.1) \times 10^6$ (0.272 ± 0.009) dB/cm	$(3.8 \pm 0.2) \times 10^6$ (0.24 ± 0.01) dB/cm	N/A
1000	$(6.7 \pm 0.4) \times 10^6$ (0.138 ± 0.008) dB/cm	$(4.5 \pm 0.4) \times 10^6$ (0.21 ± 0.02) dB/cm	$(3.9 \pm 0.1) \times 10^6$ (0.236 ± 0.007) dB/cm	N/A
2000	$(5.6 \pm 0.4) \times 10^6$ (0.17 ± 0.01) dB/cm	$(7.9 \pm 0.6) \times 10^6$ (0.116 ± 0.008) dB/cm	$(1.08 \pm 0.02) \times 10^7$ (0.084 ± 0.001) dB/cm	N/A
4000	$(1.07 \pm 0.06) \times 10^7$ (0.090 ± 0.005) dB/cm	$(1.29 \pm 0.08) \times 10^7$ (0.073 ± 0.005) dB/cm	$(1.18 \pm 0.08) \times 10^7$ (0.079 ± 0.006) dB/cm	$(1.51 \pm 0.09) \times 10^7$ (0.060 ± 0.004) dB/cm

Table S6. Measured intrinsic quality factors and propagation losses for the fundamental TM mode of microresonators with varying cross-sections at 644 nm wavelength. For each pair of width and radius, the first row is the intrinsic quality factor, and the second is the propagation loss.

Width (nm) \ Radius (μm)	30	55	115	300
500	$(1.75 \pm 0.1) \times 10^6$ (0.535 ± 0.03) dB/cm	$(5.78 \pm 0.6) \times 10^5$ (1.64 ± 0.07) dB/cm	$(6.23 \pm 0.1) \times 10^5$ (1.50 ± 0.07) dB/cm	N/A
750	$(3.74 \pm 0.2) \times 10^6$ (0.25 ± 0.01) dB/cm	$(1.38 \pm 0.1) \times 10^6$ (0.678 ± 0.009) dB/cm	$(1.55 \pm 0.2) \times 10^6$ (0.601 ± 0.01) dB/cm	N/A
1000	$(3.18 \pm 0.4) \times 10^6$ (0.293 ± 0.008) dB/cm	$(5.43 \pm 0.4) \times 10^6$ (0.174 ± 0.02) dB/cm	$(5.29 \pm 0.1) \times 10^6$ (0.176 ± 0.007) dB/cm	N/A
2000	$(4.29 \pm 0.4) \times 10^6$ (0.220 ± 0.01) dB/cm	$(5.96 \pm 0.6) \times 10^6$ (0.157 ± 0.008) dB/cm	$(8.83 \pm 0.02) \times 10^6$ (0.105 ± 0.001) dB/cm	N/A
4000	$(5.6 \pm 0.2) \times 10^6$ (0.174 ± 0.008) dB/cm	$(4.9 \pm 0.2) \times 10^6$ (0.19 ± 0.01) dB/cm	$(8.7 \pm 0.3) \times 10^6$ (0.108 ± 0.005) dB/cm	$(1.4 \pm 0.1) \times 10^7$ (0.067 ± 0.005) dB/cm

Table S7. Measured intrinsic quality factors and propagation losses for the fundamental TE mode of microresonators with varying cross-sections at 532 nm wavelength. For each pair of width and radius, the first row is the intrinsic quality factor, and the second is the propagation loss.

Width (nm) \ Radius (μm)	55	115	300
500	$(1.2 \pm 0.2) \times 10^6$ (1.0 ± 0.1) dB/cm	$(8.5 \pm 0.9) \times 10^5$ (1.3 ± 0.2) dB/cm	N/A
750	$(2.3 \pm 0.1) \times 10^6$ (0.49 ± 0.03) dB/cm	$(1.9 \pm 0.2) \times 10^6$ (0.59 ± 0.06) dB/cm	N/A
1000	$(3.4 \pm 0.3) \times 10^6$ (0.33 ± 0.03) dB/cm	$(2.9 \pm 0.2) \times 10^6$ (0.38 ± 0.02) dB/cm	N/A
2000	$(4.4 \pm 0.3) \times 10^6$ (0.26 ± 0.01) dB/cm	$(4.9 \pm 0.2) \times 10^6$ (0.232 ± 0.008) dB/cm	N/A
4000	N/A	N/A	$(5.7 \pm 0.3) \times 10^6$ (0.20 ± 0.01) dB/cm

Table S8. Measured intrinsic quality factors and propagation losses for the fundamental TM mode of microresonators with varying cross-sections at 532 nm wavelength. For each pair of width and radius, the first row is the intrinsic quality factor, and the second is the propagation loss.

Width (nm) \ Radius (μm)	55	115	300
500	$(4.6 \pm 0.2) \times 10^5$ $(2.5 \pm 0.1) \text{ dB/cm}$	$(9 \pm 2) \times 10^5$ $(1.4 \pm 0.2) \text{ dB/cm}$	N/A
750	$(1.2 \pm 0.1) \times 10^6$ $(0.9 \pm 0.1) \text{ dB/cm}$	$(1.38 \pm 0.06) \times 10^6$ $(0.83 \pm 0.04) \text{ dB/cm}$	N/A
1000	$(1.5 \pm 0.3) \times 10^6$ $(0.8 \pm 0.2) \text{ dB/cm}$	$(1.9 \pm 0.3) \times 10^6$ $(0.6 \pm 0.1) \text{ dB/cm}$	N/A
2000	$(2.4 \pm 0.2) \times 10^6$ $(0.49 \pm 0.03) \text{ dB/cm}$	$(3.6 \pm 0.2) \times 10^6$ $(0.32 \pm 0.02) \text{ dB/cm}$	N/A
4000	N/A	N/A	$(5.6 \pm 0.4) \times 10^6$ $(0.20 \pm 0.01) \text{ dB/cm}$

Table S9. Measured intrinsic quality factors and propagation losses for the fundamental TE mode of microresonators with varying cross-sections at 488 nm wavelength. For each pair of width and radius, the first row is the intrinsic quality factor, and the second is the propagation loss.

Width (nm) \ Radius (μm)	30	55	115	300
400	$(2.45 \pm 0.02) \times 10^5$ $(5.18 \pm 0.04) \text{ dB/cm}$	$(2.71 \pm 0.05) \times 10^5$ $(4.69 \pm 0.08) \text{ dB/cm}$	$(3.16 \pm 0.09) \times 10^5$ $(4.0 \pm 0.1) \text{ dB/cm}$	N/A
500	$(4.9 \pm 0.2) \times 10^5$ $(2.6 \pm 0.1) \text{ dB/cm}$	$(3.7 \pm 0.1) \times 10^5$ $(3.4 \pm 0.1) \text{ dB/cm}$	$(3.8 \pm 0.2) \times 10^5$ $(3.3 \pm 0.2) \text{ dB/cm}$	N/A
750	$(7.1 \pm 0.2) \times 10^5$ $(1.76 \pm 0.06) \text{ dB/cm}$	$(7.5 \pm 0.4) \times 10^5$ $(1.7 \pm 0.1) \text{ dB/cm}$	$(7.8 \pm 0.6) \times 10^5$ $(1.6 \pm 0.1) \text{ dB/cm}$	N/A
1000	$(7.3 \pm 0.3) \times 10^5$ $(1.72 \pm 0.07) \text{ dB/cm}$	$(8.7 \pm 0.6) \times 10^5$ $(1.44 \pm 0.09) \text{ dB/cm}$	$(9.8 \pm 0.6) \times 10^5$ $(1.27 \pm 0.07) \text{ dB/cm}$	N/A
2000	$(7.9 \pm 0.3) \times 10^5$ $(1.60 \pm 0.06) \text{ dB/cm}$	$(9.9 \pm 0.5) \times 10^5$ $(1.26 \pm 0.07) \text{ dB/cm}$	$(9.4 \pm 0.5) \times 10^5$ $(1.32 \pm 0.07) \text{ dB/cm}$	N/A
4000	$(8.4 \pm 0.4) \times 10^5$ $(1.57 \pm 0.09) \text{ dB/cm}$	$(9.3 \pm 0.5) \times 10^5$ $(1.37 \pm 0.07) \text{ dB/cm}$	$(1.03 \pm 0.05) \times 10^6$ $(1.22 \pm 0.05) \text{ dB/cm}$	$(1.0 \pm 0.1) \times 10^6$ $(1.2 \pm 0.1) \text{ dB/cm}$

Table S10. Measured intrinsic quality factors and propagation losses for the fundamental TM mode of microresonators with varying cross-sections at 488 nm wavelength. For each pair of width and radius, the first row is the intrinsic quality factor, and the second is the propagation loss.

Width (nm) \ Radius (μm)	30	55	115	300
400	$(1.34 \pm 0.03) \times 10^5$ $(9.5 \pm 0.2) \text{ dB/cm}$	$(1.65 \pm 0.05) \times 10^5$ $(7.8 \pm 0.2) \text{ dB/cm}$	$(2.9 \pm 0.2) \times 10^5$ $(4.4 \pm 0.4) \text{ dB/cm}$	N/A
500	$(2.7 \pm 0.1) \times 10^5$ $(4.8 \pm 0.2) \text{ dB/cm}$	$(2.29 \pm 0.04) \times 10^5$ $(5.6 \pm 0.1) \text{ dB/cm}$	$(2.1 \pm 0.1) \times 10^5$ $(5.9 \pm 0.4) \text{ dB/cm}$	N/A
750	$(4.46 \pm 0.08) \times 10^5$ $(2.85 \pm 0.05) \text{ dB/cm}$	$(5.4 \pm 0.2) \times 10^5$ $(2.33 \pm 0.09) \text{ dB/cm}$	$(5.2 \pm 0.2) \times 10^5$ $(2.4 \pm 0.1) \text{ dB/cm}$	N/A
1000	$(6.4 \pm 0.2) \times 10^5$ $(1.99 \pm 0.07) \text{ dB/cm}$	$(6.8 \pm 0.4) \times 10^5$ $(1.9 \pm 0.1) \text{ dB/cm}$	$(6.6 \pm 0.3) \times 10^5$ $(1.91 \pm 0.09) \text{ dB/cm}$	N/A
2000	$(6.2 \pm 0.2) \times 10^5$ $(2.09 \pm 0.07) \text{ dB/cm}$	$(7.0 \pm 0.1) \times 10^5$ $(1.82 \pm 0.04) \text{ dB/cm}$	$(8.2 \pm 0.4) \times 10^5$ $(1.55 \pm 0.08) \text{ dB/cm}$	N/A
4000	$(7.4 \pm 0.4) \times 10^5$ $(1.79 \pm 0.09) \text{ dB/cm}$	$(9.1 \pm 0.4) \times 10^5$ $(1.42 \pm 0.07) \text{ dB/cm}$	$(8.8 \pm 0.1) \times 10^5$ $(1.45 \pm 0.02) \text{ dB/cm}$	$(9.6 \pm 0.3) \times 10^5$ $(1.32 \pm 0.04) \text{ dB/cm}$

Table S11. Measured intrinsic quality factors and propagation losses for the fundamental TE mode of microresonators with varying cross-sections at 461 nm wavelength. For each pair of width and radius, the first row is the intrinsic quality factor, and the second is the propagation loss.

Width (nm) \ Radius (μm)	30	55	115
400	$(2.51 \pm 0.06) \times 10^5$ $(5.4 \pm 0.1) \text{ dB/cm}$	$(2.06 \pm 0.07) \times 10^5$ $(6.6 \pm 0.3) \text{ dB/cm}$	$(2.1 \pm 0.2) \times 10^5$ $(6.5 \pm 0.5) \text{ dB/cm}$
500	$(3.1 \pm 0.2) \times 10^5$ $(4.4 \pm 0.3) \text{ dB/cm}$	$(2.4 \pm 0.2) \times 10^5$ $(5.6 \pm 0.4) \text{ dB/cm}$	$(2.9 \pm 0.3) \times 10^5$ $(4.7 \pm 0.5) \text{ dB/cm}$
750	$(3.6 \pm 0.4) \times 10^5$ $(3.8 \pm 0.4) \text{ dB/cm}$	$(4.2 \pm 0.1) \times 10^5$ $(3.2 \pm 0.1) \text{ dB/cm}$	$(4.3 \pm 0.5) \times 10^5$ $(3.2 \pm 0.4) \text{ dB/cm}$
1000	$(4.6 \pm 0.4) \times 10^5$ $(2.9 \pm 0.3) \text{ dB/cm}$	N/A	N/A
2000	$(5.1 \pm 0.2) \times 10^5$ $(2.66 \pm 0.09) \text{ dB/cm}$	$(5.2 \pm 0.3) \times 10^5$ $(2.6 \pm 0.1) \text{ dB/cm}$	$(5.3 \pm 0.4) \times 10^5$ $(2.5 \pm 0.2) \text{ dB/cm}$
4000	$(5.2 \pm 0.5) \times 10^5$ $(2.7 \pm 0.2) \text{ dB/cm}$	$(5.3 \pm 0.5) \times 10^5$ $(2.5 \pm 0.2) \text{ dB/cm}$	$(5.6 \pm 0.5) \times 10^5$ $(2.4 \pm 0.2) \text{ dB/cm}$

Table S12. Measured intrinsic quality factors and propagation losses for the fundamental TM mode of microresonators with varying cross-sections at 461 nm wavelength. For each pair of width and radius, the first row is the intrinsic quality factor, and the second is the propagation loss.

Width (nm) \ Radius (μm)	30	55	115
400	$(1.23 \pm 0.02) \times 10^5$ $(11.2 \pm 0.2) \text{ dB/cm}$	$(1.64 \pm 0.04) \times 10^5$ $(8.4 \pm 0.3) \text{ dB/cm}$	$(1.93 \pm 0.05) \times 10^5$ $(7.1 \pm 0.2) \text{ dB/cm}$
500	$(1.80 \pm 0.09) \times 10^5$ $(7.6 \pm 0.4) \text{ dB/cm}$	$(2.1 \pm 0.1) \times 10^5$ $(6.5 \pm 0.3) \text{ dB/cm}$	$(2.2 \pm 0.1) \times 10^5$ $(6.1 \pm 0.3) \text{ dB/cm}$
750	$(3.0 \pm 0.4) \times 10^5$ $(4.5 \pm 0.2) \text{ dB/cm}$	$(3.30 \pm 0.02) \times 10^5$ $(4.11 \pm 0.03) \text{ dB/cm}$	$(3.6 \pm 0.2) \times 10^5$ $(3.8 \pm 0.3) \text{ dB/cm}$
1000	$(4.1 \pm 0.2) \times 10^5$ $(3.3 \pm 0.1) \text{ dB/cm}$	N/A	N/A
2000	$(4.3 \pm 0.2) \times 10^5$ $(3.2 \pm 0.2) \text{ dB/cm}$	$(4.9 \pm 0.6) \times 10^5$ $(2.8 \pm 0.3) \text{ dB/cm}$	$(4.7 \pm 0.1) \times 10^5$ $(2.85 \pm 0.08) \text{ dB/cm}$
4000	$(3.3 \pm 0.1) \times 10^5$ $(4.2 \pm 0.1) \text{ dB/cm}$	$(4.8 \pm 0.4) \times 10^5$ $(2.9 \pm 0.2) \text{ dB/cm}$	$(5.1 \pm 0.5) \times 10^5$ $(2.7 \pm 0.3) \text{ dB/cm}$

5. MODEL AND EXTRACTION OF ABSORPTION AND SCATTERING LOSSES

A. Total propagation loss

For each wavelength, we choose the fundamental TM mode of the waveguide with narrowest width and smallest radius as reference. The total propagation loss coefficient of this mode is

$$\alpha^{(0)} = \alpha_{abs} + \alpha_{sides} + \alpha_{top} + \alpha_{bottom} \quad (\text{S4})$$

where α_{abs} , α_{sides} , α_{top} and α_{bottom} correspond to the absorption, sidewalls scattering, top wall scattering, and bottom wall scattering contributions respectively. For another optical mode indexed by (n) , the propagation loss is

$$\alpha^{(n)} = \eta_{abs}^{(n)} \alpha_{abs} + \eta_{sides}^{(n)} \alpha_{sides} + \eta_{top}^{(n)} \alpha_{top} + \eta_{bottom}^{(n)} \alpha_{bottom} \quad (\text{S5})$$

where

$$P^{(n)} = \iint S_\phi^{(n)} dA \quad (\text{S6})$$

$$C^{(n)} = \frac{1}{P^{(n)}} \iint_{core} S_\phi^{(n)} dA \quad (\text{S7})$$

$$S_\phi^{(n)} = \frac{1}{P^{(n)}} \int_{sides} S_\phi^{(n)} dl \quad (\text{S8})$$

$$T^{(n)} = \frac{1}{P^{(n)}} \int_{top} S_\phi^{(n)} dl \quad (\text{S9})$$

$$B^{(n)} = \frac{1}{P^{(n)}} \int_{bottom} S_\phi^{(n)} dl \quad (\text{S10})$$

$$\eta_{abs}^{(n)} = \frac{C^{(n)}}{C^{(0)}} \quad (\text{S11})$$

$$\eta_{sides}^{(n)} = \frac{S^{(n)}}{S^{(0)}} \quad (S12)$$

$$\eta_{top}^{(n)} = \frac{T^{(n)}}{T^{(0)}} \quad (S13)$$

$$\eta_{bottom}^{(n)} = \frac{B^{(n)}}{B^{(0)}} \quad (S14)$$

$S_\phi^{(n)}$ is the Poynting vector of the mode in the propagation direction, $P^{(n)}$ is the optical power, $C^{(n)}$ is the confinement factor, $S^{(n)}$ is the overlap with the sidewalls, $T^{(n)}$ is the overlap with the top wall, and $B^{(n)}$ is the overlap with the bottom wall. The factors $\eta_{abs}^{(n)}$, $\eta_{sides}^{(n)}$, $\eta_{top}^{(n)}$ and $\eta_{bottom}^{(n)}$ refer to the aforementioned quantities relative to the reference optical mode. Tables S13 to S22 summarize the values of these quantities for the fundamental TE and TM modes of all the microresonators geometries and wavelengths measured experimentally.

We extract α_{sides} and α_{abs} from fitting the data presented in Fig. 2b of the main text and Fig. S2 using Eq. (S5). Since the top and bottom walls are about at least an order of magnitude smoother than the sidewalls (section 5C), we consider that $\alpha_{top} \approx \alpha_{bottom} \approx 0$. If we had kept α_{top} and α_{bottom} as free parameters or had estimated them using the model presented in section 5C, the determination of α_{abs} would have been subject to uncertainty. Since only $\eta_{sides}^{(n)}$ varies significantly for the different waveguide geometries (Tables S13 to S22), the non-zero top and bottom scattering losses would have acted as an effective absorption loss, thus lowering the α_{abs} obtained from the fittings. By neglecting α_{top} and α_{bottom} , we extract an α_{abs} that represents an upper bound for the material absorption.

As a final comment, it is worth noting that α_{abs} and $(\alpha_{sides}, \alpha_{top}, \alpha_{bottom})$ phenomenologically encompass any sources of loss that relate to the volume and the surface of the waveguides, respectively. For example, if the film contained a volumetric density of voids or defects, α_{abs} would represent the sum of absorption and volumetric Rayleigh scattering. In our case, however, absorption is the dominant volumetric loss, as the films do not present visible voids or defects (Fig. S1).

Table S13. Confinement, overlaps and coefficients for the fundamental TE mode of microresonators with varying cross-sections at 780 nm wavelength. For each pair of width and radius, the rows read as: $C^{(n)} \left(\eta_{abs}^{(n)} \right)$ for the first, $S^{(n)}$ in $1/m \left(\eta_{sides}^{(n)} \right)$ for the second, and $T^{(n)}$ in $1/m \left(\eta_{top}^{(n)} \right)$ for the third. Since the cladding is symmetric, $B^{(n)} = T^{(n)}$ and $\eta_{top}^{(n)} = \eta_{bottom}^{(n)}$.

Width (nm) \ Radius (μm)	55	115	300
500	0.7659 (0.9432)	0.7660 (0.9434)	0.7661 (0.9434)
	617266 (2.8651)	616664 (2.8739)	616581 (2.8800)
	1376498 (0.9610)	1376683 (0.9612)	1376729 (0.9612)
750	0.8120 (1.0000)	0.8122 (1.0002)	0.8122 (1.0003)
	217893 (1.0000)	216722 (1.0045)	216459 (1.0090)
	1432286 (1.0000)	1432502 (1.0002)	1432556 (1.0002)
1000	0.8242 (1.0150)	0.8245 (1.0153)	0.8245 (1.0154)
	101566 (0.4570)	99406 (0.4563)	98869 (0.4591)
	1446833 (1.0102)	1447163 (1.0104)	1447246 (1.0104)
2000	0.8316 (1.0241)	0.8326 (1.0254)	0.8330 (1.0258)
	27941 (0.1137)	17708 (0.0747)	14558 (0.0650)
	1455653 (1.0163)	1456927 (1.0172)	1457316 (1.0175)
4000	0.8318 (1.0243)	0.8332 (1.0260)	0.8339 (1.0270)
	25996 (0.1049)	12446 (0.0502)	4841 (0.0196)
	1455884 (1.0165)	1457542 (1.0176)	1458448 (1.0183)

Table S14. Confinement, overlaps and coefficients for the fundamental TM mode of microresonators with varying cross-sections at 780 nm wavelength. For each pair of width and radius, the rows read as: $C^{(n)} \left(\eta_{abs}^{(n)} \right)$ for the first, $S^{(n)}$ in $1/m \left(\eta_{sides}^{(n)} \right)$ for the second, and $T^{(n)}$ in $1/m \left(\eta_{top}^{(n)} \right)$ for the third. Since the cladding is symmetric, $B^{(n)} = T^{(n)}$ and $\eta_{top}^{(n)} = \eta_{bottom}^{(n)}$.

Width (nm) \ Radius (μm)	55	115	300
500	0.7659 (0.9432)	0.7660 (0.9434)	0.7661 (0.9434)
	617266 (2.8651)	616664 (2.8739)	616581 (2.8800)
	1376498 (0.9610)	1376683 (0.9612)	1376729 (0.9612)
750	0.8120 (1.0000)	0.8122 (1.0002)	0.8122 (1.0003)
	217893 (1.0000)	216722 (1.0045)	216459 (1.0090)
	1432286 (1.0000)	1432502 (1.0002)	1432556 (1.0002)
1000	0.8242 (1.0150)	0.8245 (1.0153)	0.8245 (1.0154)
	101566 (0.4570)	99406 (0.4563)	98869 (0.4591)
	1446833 (1.0102)	1447163 (1.0104)	1447246 (1.0104)
2000	0.8285 (1.0203)	0.8286 (1.0204)	0.8285 (1.0203)
	58492 (0.2703)	57831 (0.2618)	57350 (0.2500)
	1451968 (1.0137)	1452007 (1.0138)	1451914 (1.0137)
4000	0.8290 (1.0209)	0.8291 (1.0210)	0.8314 (1.0238)
	52125 (0.2402)	50621 (0.2274)	27997 (0.1131)
	1452448 (1.0141)	1452535 (1.0141)	1455351 (1.0161)

Table S15. Confinement, overlaps and coefficients for the fundamental TE mode of microresonators with varying cross-sections at 644 nm wavelength. For each pair of width and radius, the rows read as: $C^{(n)} \left(\eta_{abs}^{(n)} \right)$ for the first, $S^{(n)}$ in $1/m \left(\eta_{sides}^{(n)} \right)$ for the second, and $T^{(n)}$ in $1/m \left(\eta_{top}^{(n)} \right)$ for the third. Since the cladding is symmetric, $B^{(n)} = T^{(n)}$ and $\eta_{top}^{(n)} = \eta_{bottom}^{(n)}$.

Width (nm) \ Radius (μm)	30	55	115	300
500	0.8545 (1.0338)	0.8547 (1.0341)	0.8548 (1.0342)	0.8548 (1.0342)
	454978 (0.6190)	453088 (0.6214)	452458 (0.6237)	452292 (0.6253)
	1252204 (1.2241)	1252415 (1.2243)	1252489 (1.2244)	1252503 (1.2244)
750	0.8774 (1.0615)	0.8778 (1.0620)	0.8779 (1.0622)	0.8779 (1.0622)
	157005 (0.2074)	152613 (0.2059)	151120 (0.2067)	150781 (0.2078)
	1271485 (1.2429)	1271837 (1.2433)	1271951 (1.2434)	1271979 (1.2434)
1000	0.8829 (1.0683)	0.8836 (1.0691)	0.8839 (1.0694)	0.8839 (1.0695)
	80040 (0.1011)	71301 (0.0934)	68328 (0.0921)	67591 (0.0926)
	1276217 (1.2475)	1276822 (1.2481)	1277027 (1.2483)	1277080 (1.2484)
2000	0.8851 (1.0709)	0.8867 (1.0729)	0.8876 (1.0740)	0.8879 (1.0743)
	48703 (0.0580)	26734 (0.0319)	14522 (0.0177)	10147 (0.0131)
	1278117 (1.2494)	1279513 (1.2508)	1280273 (1.2515)	1280542 (1.2518)
4000	0.8852 (1.0711)	0.8868 (1.0730)	0.8878 (1.0741)	0.8883 (1.0748)
	47131 (0.0561)	25993 (0.0310)	12485 (0.0149)	4794 (0.0057)
	1278220 (1.2495)	1279562 (1.2508)	1280396 (1.2516)	1280864 (1.2521)

Table S16. Confinement, overlaps and coefficients for the fundamental TM mode of microresonators with varying cross-sections at 644 nm wavelength. For each pair of width and radius, the rows read as: $C^{(n)} \left(\eta_{abs}^{(n)} \right)$ for the first, $S^{(n)}$ in $1/m \left(\eta_{sides}^{(n)} \right)$ for the second, and $T^{(n)}$ in $1/m \left(\eta_{top}^{(n)} \right)$ for the third. Since the cladding is symmetric, $B^{(n)} = T^{(n)}$ and $\eta_{top}^{(n)} = \eta_{bottom}^{(n)}$.

Width (nm) \ Radius (μm)	30	55	115	300
500	0.8265 (1.0000)	0.8268 (1.0004)	0.8269 (1.0005)	0.8270 (1.0006)
	736413 (1.0000)	733282 (1.0047)	732270 (1.0090)	732004 (1.0118)
	1022980 (1.0000)	1023356 (1.0004)	1023332 (1.0003)	1023425 (1.0004)
750	0.8525 (1.0315)	0.8532 (1.0324)	0.8535 (1.0326)	0.8535 (1.0327)
	300497 (0.3950)	290984 (0.3914)	287829 (0.3931)	287024 (0.3954)
	1041541 (1.0181)	1041981 (1.0186)	1042199 (1.0188)	1042231 (1.0188)
1000	0.8599 (1.0405)	0.8612 (1.0420)	0.8617 (1.0426)	0.8618 (1.0427)
	168675 (0.2119)	148642 (0.1940)	141754 (0.1906)	139978 (0.1917)
	1046876 (1.0234)	1047772 (1.0242)	1048145 (1.0246)	1048206 (1.0247)
2000	0.8630 (1.0442)	0.8659 (1.0476)	0.8675 (1.0496)	0.8681 (1.0503)
	112318 (0.1338)	63150 (0.0753)	34537 (0.0420)	23900 (0.0308)
	1049082 (1.0255)	1051184 (1.0276)	1052443 (1.0288)	1052818 (1.0292)
4000	0.8632 (1.0444)	0.8660 (1.0477)	0.8677 (1.0499)	0.8687 (1.0511)
	108833 (0.1297)	61519 (0.0733)	30137 (0.0359)	11750 (0.0140)
	1049224 (1.0257)	1051202 (1.0276)	1052564 (1.0289)	1053254 (1.0296)

Table S17. Confinement, overlaps and coefficients for the fundamental TE mode of microresonators with varying cross-sections at 532 nm wavelength. For each pair of width and radius, the rows read as: $C^{(n)} \left(\eta_{abs}^{(n)} \right)$ for the first, $S^{(n)}$ in $1/m \left(\eta_{sides}^{(n)} \right)$ for the second, and $T^{(n)}$ in $1/m \left(\eta_{top}^{(n)} \right)$ for the third. Since the cladding is symmetric, $B^{(n)} = T^{(n)}$ and $\eta_{top}^{(n)} = \eta_{bottom}^{(n)}$.

Width (nm) \ Radius (μm)	55	115	300
500	0.9086 (1.0091) 323648 (0.5586) 1072951 (1.3563)	0.9087 (1.0091) 322941 (0.5600) 1072982 (1.3564)	0.9087 (1.0091) 322775 (0.5613) 1072991 (1.3564)
	0.9205 (1.0222) 107165 (0.1818) 1079883 (1.3651)	0.9206 (1.0224) 105223 (0.1810) 1079950 (1.3652)	0.9206 (1.0224) 104652 (0.1814) 1079969 (1.3652)
	0.9234 (1.0255) 51549 (0.0850) 1081652 (1.3673)	0.9236 (1.0257) 47514 (0.0805) 1081789 (1.3675)	0.9237 (1.0258) 46464 (0.0801) 1081825 (1.3675)
1000	0.9247 (1.0269) 26297 (0.0412) 1082464 (1.3683)	0.9254 (1.0277) 13085 (0.0206) 1082894 (1.3689)	0.9257 (1.0280) 7476 (0.0122) 1083076 (1.3691)
	0.9247 (1.0269) 25772 (0.0403) 1082480 (1.3684)	0.9254 (1.0277) 12406 (0.0194) 1082916 (1.3689)	0.9258 (1.0282) 4764 (0.0075) 1083164 (1.3692)
2000			
4000			

Table S18. Confinement, overlaps and coefficients for the fundamental TM mode of microresonators with varying cross-sections at 532 nm wavelength. For each pair of width and radius, the rows read as: $C^{(n)} \left(\eta_{abs}^{(n)} \right)$ for the first, $S^{(n)}$ in $1/m \left(\eta_{sides}^{(n)} \right)$ for the second, and $T^{(n)}$ in $1/m \left(\eta_{top}^{(n)} \right)$ for the third. Since the cladding is symmetric, $B^{(n)} = T^{(n)}$ and $\eta_{top}^{(n)} = \eta_{bottom}^{(n)}$.

Width (nm) \ Radius (μm)	55	115	300
500	0.9005 (1.0000) 580104 (1.0000) 791079 (1.0000)	0.9006 (1.0001) 578603 (1.0028) 791075 (1.0000)	0.9006 (1.0001) 578230 (1.0053) 791097 (1.0000)
	0.9152 (1.0163) 219716 (0.3717) 797571 (1.0082)	0.9154 (1.0166) 215111 (0.3694) 797659 (1.0083)	0.9154 (1.0166) 213940 (0.3706) 797735 (1.0084)
	0.9193 (1.0209) 114089 (0.1875) 799616 (1.0108)	0.9197 (1.0214) 104080 (0.1759) 799767 (1.0110)	0.9198 (1.0215) 101467 (0.1747) 799802 (1.0110)
1000	0.9212 (1.0230) 63760 (0.0998) 800590 (1.0120)	0.9225 (1.0244) 32102 (0.0504) 801244 (1.0128)	0.9230 (1.0250) 18154 (0.0295) 801459 (1.0131)
	0.9213 (1.0231) 62588 (0.0979) 800604 (1.0120)	0.9225 (1.0245) 30647 (0.0480) 801184 (1.0128)	0.9233 (1.0253) 11921 (0.0187) 801510 (1.0132)

Table S19. Confinement, overlaps and coefficients for the fundamental TE mode of microresonators with varying cross-sections at 488 nm wavelength. For each pair of width and radius, the rows read as: $C^{(n)} \left(\eta_{abs}^{(n)} \right)$ for the first, $S^{(n)}$ in $1/m \left(\eta_{sides}^{(n)} \right)$ for the second, and $T^{(n)}$ in $1/m \left(\eta_{top}^{(n)} \right)$ for the third. Since the cladding is symmetric, $B^{(n)} = T^{(n)}$ and $\eta_{top}^{(n)} = \eta_{bottom}^{(n)}$.

Width (nm) \ Radius (μm)	30	55	115	300
400	0.9156 (1.0048) 503441 (0.5848) 974815 (1.4317)	0.9157 (1.0050) 501921 (0.5866) 974868 (1.4318)	0.9158 (1.0050) 501407 (0.5883) 974888 (1.4318)	0.9158 (1.0050) 501260 (0.5894) 974891 (1.4318)
	0.9269 (1.0172) 275745 (0.3171) 980129 (1.4395)	0.9271 (1.0174) 273223 (0.3175) 980208 (1.4396)	0.9271 (1.0175) 272393 (0.3187) 980230 (1.4396)	0.9271 (1.0175) 272174 (0.3197) 980236 (1.4397)
	0.9354 (1.0265) 96962 (0.1070) 984316 (1.4457)	0.9357 (1.0269) 90258 (0.1024) 984487 (1.4459)	0.9358 (1.0270) 88027 (0.1018) 984544 (1.4460)	0.9358 (1.0271) 87469 (0.1023) 984558 (1.4460)
750	0.9372 (1.0285) 57646 (0.0608) 985254 (1.4470)	0.9378 (1.0292) 44601 (0.0487) 985575 (1.4475)	0.9380 (1.0294) 39921 (0.0452) 985691 (1.4477)	0.9381 (1.0295) 38696 (0.0449) 985719 (1.4477)
	0.9376 (1.0290) 47772 (0.0493) 985494 (1.4474)	0.9386 (1.0301) 26079 (0.0269) 986024 (1.4482)	0.9392 (1.0308) 12714 (0.0132) 986349 (1.4486)	0.9395 (1.0311) 6593 (0.0071) 986499 (1.4489)
	0.9377 (1.0291) 46220 (0.0477) 985531 (1.4474)	0.9386 (1.0301) 25597 (0.0264) 986035 (1.4482)	0.9393 (1.0308) 12333 (0.0127) 986358 (1.4486)	0.9396 (1.0312) 4739 (0.0049) 986545 (1.4489)
1000	0.9372 (1.0285) 57646 (0.0608) 985254 (1.4470)	0.9378 (1.0292) 44601 (0.0487) 985575 (1.4475)	0.9380 (1.0294) 39921 (0.0452) 985691 (1.4477)	0.9381 (1.0295) 38696 (0.0449) 985719 (1.4477)
	0.9376 (1.0290) 47772 (0.0493) 985494 (1.4474)	0.9386 (1.0301) 26079 (0.0269) 986024 (1.4482)	0.9392 (1.0308) 12714 (0.0132) 986349 (1.4486)	0.9395 (1.0311) 6593 (0.0071) 986499 (1.4489)
	0.9377 (1.0291) 46220 (0.0477) 985531 (1.4474)	0.9386 (1.0301) 25597 (0.0264) 986035 (1.4482)	0.9393 (1.0308) 12333 (0.0127) 986358 (1.4486)	0.9396 (1.0312) 4739 (0.0049) 986545 (1.4489)
2000	0.9376 (1.0290) 47772 (0.0493) 985494 (1.4474)	0.9386 (1.0301) 26079 (0.0269) 986024 (1.4482)	0.9392 (1.0308) 12714 (0.0132) 986349 (1.4486)	0.9395 (1.0311) 6593 (0.0071) 986499 (1.4489)
	0.9377 (1.0291) 46220 (0.0477) 985531 (1.4474)	0.9386 (1.0301) 25597 (0.0264) 986035 (1.4482)	0.9393 (1.0308) 12333 (0.0127) 986358 (1.4486)	0.9396 (1.0312) 4739 (0.0049) 986545 (1.4489)
	0.9377 (1.0291) 46220 (0.0477) 985531 (1.4474)	0.9386 (1.0301) 25597 (0.0264) 986035 (1.4482)	0.9393 (1.0308) 12333 (0.0127) 986358 (1.4486)	0.9396 (1.0312) 4739 (0.0049) 986545 (1.4489)
4000	0.9377 (1.0291) 46220 (0.0477) 985531 (1.4474)	0.9386 (1.0301) 25597 (0.0264) 986035 (1.4482)	0.9393 (1.0308) 12333 (0.0127) 986358 (1.4486)	0.9396 (1.0312) 4739 (0.0049) 986545 (1.4489)
	0.9377 (1.0291) 46220 (0.0477) 985531 (1.4474)	0.9386 (1.0301) 25597 (0.0264) 986035 (1.4482)	0.9393 (1.0308) 12333 (0.0127) 986358 (1.4486)	0.9396 (1.0312) 4739 (0.0049) 986545 (1.4489)
	0.9377 (1.0291) 46220 (0.0477) 985531 (1.4474)	0.9386 (1.0301) 25597 (0.0264) 986035 (1.4482)	0.9393 (1.0308) 12333 (0.0127) 986358 (1.4486)	0.9396 (1.0312) 4739 (0.0049) 986545 (1.4489)

Table S20. Confinement, overlaps and coefficients for the fundamental TM mode of microresonators with varying cross-sections at 488 nm wavelength. For each pair of width and radius, the rows read as: $C^{(n)} \left(\eta_{abs}^{(n)} \right)$ for the first, $S^{(n)}$ in $1/m \left(\eta_{sides}^{(n)} \right)$ for the second, and $T^{(n)}$ in $1/m \left(\eta_{top}^{(n)} \right)$ for the third. Since the cladding is symmetric, $B^{(n)} = T^{(n)}$ and $\eta_{top}^{(n)} = \eta_{bottom}^{(n)}$.

Width (nm) \ Radius (μm)	30	55	115	300
400	0.9112 (1.0000) 862379 (1.0000) 680881 (1.0000)	0.9113 (1.0002) 859482 (1.0036) 680953 (1.0001)	0.9114 (1.0002) 858543 (1.0069) 680942 (1.0001)	0.9114 (1.0002) 858304 (1.0091) 681009 (1.0002)
	0.9237 (1.0138) 516417 (0.5921) 685240 (1.0064)	0.9240 (1.0141) 510993 (0.5929) 685322 (1.0065)	0.9241 (1.0142) 509217 (0.5954) 685362 (1.0066)	0.9241 (1.0142) 508763 (0.5974) 685336 (1.0065)
	0.9345 (1.0256) 207523 (0.2277) 689388 (1.0125)	0.9351 (1.0263) 191187 (0.2160) 689586 (1.0128)	0.9353 (1.0265) 185676 (0.2143) 689631 (1.01285)	0.9354 (1.0266) 184265 (0.2153) 689658 (1.0129)
750	0.9370 (1.0283) 133603 (0.1404) 690426 (1.0140)	0.9381 (1.0296) 101574 (0.1103) 690816 (1.0146)	0.9385 (1.0300) 89698 (0.1012) 691004 (1.0149)	0.9387 (1.0302) 86557 (0.1002) 691032 (1.0149)
	0.9376 (1.0290) 115111 (0.1188) 690699 (1.0144)	0.9394 (1.0309) 64142 (0.0662) 691419 (1.0155)	0.9405 (1.0321) 31683 (0.0328) 691812 (1.0161)	0.9410 (1.0327) 16290 (0.0174) 692086 (1.0165)
	0.9377 (1.0291) 111559 (0.1152) 690703 (1.0144)	0.9394 (1.0310) 63008 (0.0651) 691362 (1.0154)	0.9405 (1.0322) 30847 (0.0318) 691858 (1.0161)	0.9411 (1.0329) 11996 (0.0124) 692199 (1.0166)

Table S21. Confinement, overlaps and coefficients for the fundamental TE mode of microresonators with varying cross-sections at 461 nm wavelength. For each pair of width and radius, the rows read as: $C^{(n)} \left(\eta_{abs}^{(n)} \right)$ for the first, $S^{(n)}$ in $1/m \left(\eta_{sides}^{(n)} \right)$ for the second, and $T^{(n)}$ in $1/m \left(\eta_{top}^{(n)} \right)$ for the third. Since the cladding is symmetric, $B^{(n)} = T^{(n)}$ and $\eta_{top}^{(n)} = \eta_{bottom}^{(n)}$.

Width (nm) \ Radius (μm)	30	55	115	300
400	0.9281 (1.0023)	0.9282 (1.0025)	0.9283 (1.0025)	0.9283 (1.0025)
	449986 (0.5665)	448281 (0.5685)	447745 (0.5705)	447704 (0.5720)
	913454 (1.4850)	913498 (1.4851)	913511 (1.4851)	913514 (1.4851)
500	0.9373 (1.0122)	0.9375 (1.0124)	0.9375 (1.0125)	0.9375 (1.0125)
	245650 (0.3054)	242964 (0.3060)	242045 (0.3074)	241804 (0.3085)
	917280 (1.4913)	917338 (1.4914)	917361 (1.4914)	917365 (1.4914)
750	0.9441 (1.0196)	0.9444 (1.0200)	0.9446 (1.0201)	0.9446 (1.0201)
	87783 (0.1038)	80394 (0.0982)	77937 (0.0975)	77298 (0.0981)
	920309 (1.4962)	920457 (1.4964)	920507 (1.4965)	920519 (1.4965)
1000	0.9455 (1.0211)	0.9461 (1.0217)	0.9463 (1.0220)	0.9464 (1.0221)
	54749 (0.0617)	40682 (0.0475)	35506 (0.0433)	34141 (0.0429)
	920963 (1.4973)	921244 (1.4977)	921347 (1.4979)	921375 (1.4979)
2000	0.9458 (1.0214)	0.9467 (1.0224)	0.9473 (1.0230)	0.9475 (1.0233)
	47410 (0.0525)	25894 (0.0287)	12518 (0.0139)	6113 (0.0070)
	921112 (1.4975)	921544 (1.4982)	921813 (1.4986)	921944 (1.4988)
4000	0.9459 (1.0215)	0.9467 (1.0224)	0.9473 (1.0230)	0.9476 (1.0233)
	45878 (0.0508)	25419 (0.0281)	12258 (0.0136)	4711 (0.0052)
	921142 (1.4975)	921554 (1.4982)	921819 (1.4986)	921973 (1.4989)

Table S22. Confinement, overlaps and coefficients for the fundamental TM mode of microresonators with varying cross-sections at 461 nm wavelength. For each pair of width and radius, the rows read as: $C^{(n)} \left(\eta_{abs}^{(n)} \right)$ for the first, $S^{(n)}$ in $1/m \left(\eta_{sides}^{(n)} \right)$ for the second, and $T^{(n)}$ in $1/m \left(\eta_{top}^{(n)} \right)$ for the third. Since the cladding is symmetric, $B^{(n)} = T^{(n)}$ and $\eta_{top}^{(n)} = \eta_{bottom}^{(n)}$.

Width (nm) \ Radius (μm)	30	55	115	300
400	0.9260 (1.0000)	0.9261 (1.0002)	0.9262 (1.0002)	0.9262 (1.0002)
	796024 (1.0000)	792754 (1.0043)	791699 (1.0082)	791417 (1.0109)
	615103 (1.0000)	615113 (1.0000)	615192 (1.0001)	615140 (1.0001)
500	0.9365 (1.0114)	0.9368 (1.0116)	0.9368 (1.0117)	0.9369 (1.0118)
	473287 (0.5863)	467176 (0.5873)	465169 (0.5902)	464661 (0.5927)
	618451 (1.0054)	618502 (1.0055)	618506 (1.0055)	618492 (1.0055)
750	0.9453 (1.0209)	0.9460 (1.0216)	0.9462 (1.0218)	0.9462 (1.0219)
	192260 (0.2260)	173976 (0.2116)	167759 (0.2094)	166168 (0.2106)
	621509 (1.0104)	621688 (1.0107)	621711 (1.0107)	621754 (1.0108)
1000	0.9472 (1.0230)	0.9484 (1.0242)	0.9488 (1.0247)	0.9489 (1.0248)
	129365 (0.1453)	94464 (0.1097)	81187 (0.0985)	77640 (0.0973)
	622246 (1.0116)	622595 (1.0122)	622742 (1.0124)	622817 (1.0125)
2000	0.9477 (1.0234)	0.9493 (1.0252)	0.9503 (1.0263)	0.9508 (1.0268)
	115542 (0.1279)	64360 (0.0712)	31547 (0.0350)	15295 (0.0175)
	622428 (1.0119)	622936 (1.0127)	623359 (1.0134)	623572 (1.0138)
4000	0.9478 (1.0236)	0.9493 (1.0252)	0.9503 (1.0263)	0.9509 (1.0269)
	111976 (0.1239)	63233 (0.0700)	30954 (0.0343)	12037 (0.0133)
	622436 (1.0119)	622915 (1.0127)	623379 (1.0135)	623588 (1.0138)

B. Material absorption

For each wavelength, we obtain the absorption coefficient of the bulk SiN $\alpha_{abs,bulk}$ from

$$\alpha_{abs,bulk} = \frac{\alpha_{abs}}{C^{(0)}} \quad (\text{S15})$$

which accounts for the confinement of the reference optical mode. Eq. (S15) uses the fact that the SiO₂ cladding is fully transparent in the visible spectral range, with an optical bandgap about twice as large as SiN [23]. As such, the small portion of the optical mode spread in the cladding does not contribute to the absorption loss. For the ultraviolet wavelengths where we measured absorption via ellipsometry (Fig. 1a), we calculate $\alpha_{abs,bulk}$ from k using $\alpha_{abs,bulk} = 4\pi k/\lambda$.

We fit $\alpha_{abs,bulk}$ as a function of wavelength using the expression [24]

$$\alpha_{abs,bulk} = \frac{\alpha_0}{\hbar\omega} \frac{1}{\beta^2} \mathcal{J}_{cv}(\beta(\hbar\omega - E_g)) \quad (\text{S16})$$

where

$$\mathcal{J}_{cv}(z) = -\frac{\pi}{4} \text{Li}_2(-e^z) \quad (\text{S17})$$

and Li₂(·) is the polylogarithm of order 2. Eq. (S16) accurately models the absorption of amorphous materials simultaneously for the Tauc regime (high absorption, measured via ellipsometry) and the Urbach tail (medium absorption, measured via microring resonators).

C. Surface scattering

We model the wavelength dependence of the sidewalls scattering loss using a normalized version of the Payne-Lacey model [25, 26]. We introduce the normalization to account for the varying overlaps with the sidewalls of the reference optical modes at the different wavelengths, which creates an additional wavelength dependence for the total loss. By normalizing the model, we exclude this geometric contribution and obtain the fundamental functional form of the loss per unit of overlap as a function of wavelength.

The normalized sidewalls scattering loss coefficient is given by

$$\alpha_{sides}^{norm} = \left(n_{core}^2 - n_{clad}^2 \right)^2 \frac{k_0^3}{4\pi n_{core}} S_{sides} \quad (\text{S18})$$

where

$$S_{sides} = \sqrt{2}\sigma_{sides}^2 L_{c,sides} \pi \sqrt{\frac{\sqrt{4\beta^2 L_{c,sides}^2 + [1 - L_{c,sides}^2(\beta^2 - n_{clad}^2 k_0^2)]^2} + 1 - L_{c,sides}^2(\beta^2 - n_{clad}^2 k_0^2)}{4\beta^2 L_{c,sides}^2 + [1 - L_{c,sides}^2(\beta^2 - n_{clad}^2 k_0^2)]^2}} \quad (\text{S19})$$

and $k_0 = 2\pi/\lambda$. σ_{sides} is the root mean square (RMS) roughness, $L_{c,sides}$ is the correlation length, β is the propagation constant of the reference mode, n_{core} is the refractive index of the SiN core and n_{clad} is the refractive index of the SiO₂ cladding.

The normalization allows us to easily calculate the total sidewall scattering loss $\alpha_{sides}^{(n)}$ of any mode (n) by simply multiplying α_{sides}^{norm} by the overlap $S^{(n)}$

$$\alpha_{sides}^{(n)} = \alpha_{sides}^{norm} S^{(n)} \quad (\text{S20})$$

Similarly, we can apply the same model to the top and bottom walls, resulting in

$$\alpha_{top}^{norm} = \frac{1}{2} \left(n_{core}^2 - n_{clad}^2 \right)^2 \frac{k_0^3}{4\pi n_{core}} S_{top} \quad (\text{S21})$$

$$\alpha_{bottom}^{norm} = \frac{1}{2} \left(n_{core}^2 - n_{clad}^2 \right)^2 \frac{k_0^3}{4\pi n_{core}} S_{bottom} \quad (\text{S22})$$

with

$$S_{top} = \sqrt{2}\sigma_{top}^2 L_{c,top} \pi \sqrt{\frac{\sqrt{4\beta^2 L_{c,top}^2 + [1 - L_{c,top}^2(\beta^2 - n_{clad}^2 k_0^2)]^2} + 1 - L_{c,top}^2(\beta^2 - n_{clad}^2 k_0^2)}{4\beta^2 L_{c,top}^2 + [1 - L_{c,top}^2(\beta^2 - n_{clad}^2 k_0^2)]^2}} \quad (\text{S23})$$

$$S_{bottom} = \sqrt{2}\sigma_{bottom}^2 L_{c,bottom} \pi \sqrt{\frac{\sqrt{4\beta^2 L_{c,bottom}^2 + [1 - L_{c,bottom}^2(\beta^2 - n_{clad}^2 k_0^2)]^2} + 1 - L_{c,bottom}^2(\beta^2 - n_{clad}^2 k_0^2)}{4\beta^2 L_{c,bottom}^2 + [1 - L_{c,bottom}^2(\beta^2 - n_{clad}^2 k_0^2)]^2}} \quad (\text{S24})$$

where the RMS roughness and correlation lengths now refer to the top and bottom walls.

We include the factor 1/2 in Eq. (S21) and Eq. (S22) because each surface has their own RMS roughness and correlation length, and therefore must be considered independently [25]. The conversion from the normalized loss coefficient to the actual loss coefficient of a mode (n) follows the same principle of Eq. (S20), yielding

$$\alpha_{top}^{(n)} = \alpha_{top}^{norm} T^{(n)} \quad (\text{S25})$$

$$\alpha_{bottom}^{(n)} = \alpha_{bottom}^{norm} B^{(n)} \quad (\text{S26})$$

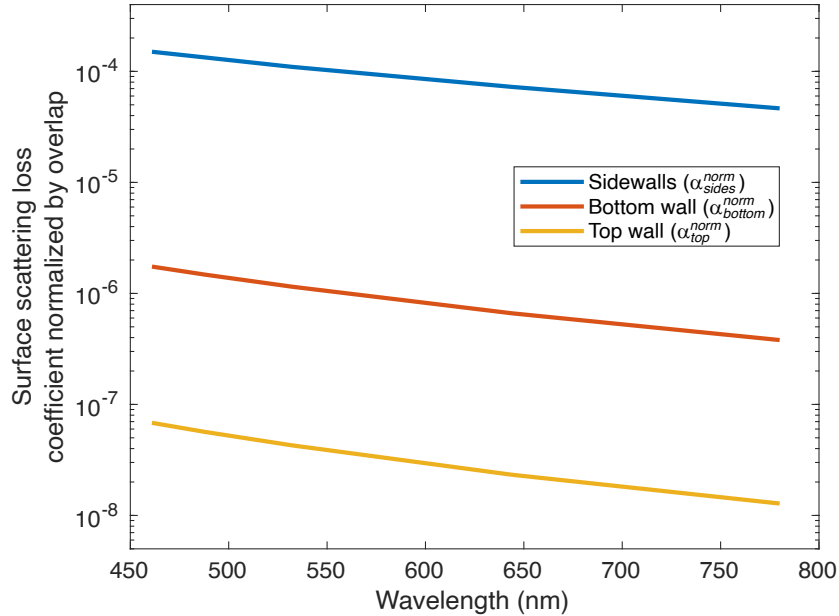


Fig. S3. Simulated surface scattering loss coefficient normalized by overlap for the top wall $\alpha_{\text{top}}^{\text{norm}}$ ($\sigma_{\text{top}} = 0.08 \text{ nm}$, $L_{c,\text{top}} = 8.76 \text{ nm}$) [27], bottom wall $\alpha_{\text{bottom}}^{\text{norm}}$ ($\sigma_{\text{bottom}} = 0.28 \text{ nm}$, $L_{c,\text{bottom}} = 23.5 \text{ nm}$) [27], and sidewalls $\alpha_{\text{sides}}^{\text{norm}}$ ($\sigma_{\text{sides}} = 1.5 \text{ nm}$, $L_{c,\text{sides}} = 90 \text{ nm}$). Since the top and bottom walls are orders of magnitude smoother than the sidewalls, the total scattering is dominated by the sidewalls.

Since the chemical-mechanical-polished top surface and the thermally-grown bottom surface are much smoother than the sidewalls [27], the scattering loss is dominated by the latter (Fig. S3), supporting the assumption that $\alpha_{\text{top}} \approx \alpha_{\text{bottom}} \approx 0$ in section 5A.

In addition to the normalized Payne-Lacey model, we also model the surface scattering loss by a simple power law of the form $\alpha_{\text{sides}}^{\text{norm}} = A\lambda^{-\gamma}$, where A is a constant that depends on the roughness. The exponent γ effectively accounts for the $k_0^3 \propto \lambda^{-3}$ dependence of the scattering and the correction provided by S_{sides} (Eq. S18), resulting in $\gamma = (2.3 \pm 0.6)$ according to our experimental data.

D. Measured absorption and surface scattering loss limits as a function of wavelength

Table S23 summarizes the absorption and surface scattering loss contributions for our integrated SiN platform as a function of wavelength, which are depicted in Fig. 4 of the main text. We extract the values from the measured microresonator losses following the models presented in the previous subsections. The errorbars of the datapoints in Fig. 4 of the main text correspond to the uncertainty from the fittings of the raw data (section 4) using the model of section 5A, while the errorbars of E_g , β , σ , and L_c correspond to the fitting uncertainties of the band-fluctuations and NPL models (sections 5B and 5C).

Table S23. Extracted absorption and normalized sidewalls scattering coefficients as a function of wavelength for our integrated SiN platform.

Wavelength (nm)	Film absorption coefficient $\alpha_{abs,bulk}$ (dB/cm)	Normalized sidewalls scattering loss coefficient α_{sides}^{norm}
780	0.02 ± 0.01	$(8 \pm 1) \times 10^{-5}$
644	0.06 ± 0.02	$(3.6 \pm 0.7) \times 10^{-5}$
532	0.20 ± 0.09	$(8 \pm 1) \times 10^{-5}$
488	1.2 ± 0.3	$(1.7 \pm 0.3) \times 10^{-4}$
461	2.49 ± 0.07	$(2.0 \pm 0.2) \times 10^{-4}$

REFERENCES

1. L. Y. Beliaev, E. Shkondin, A. V. Lavrinenko, and O. Takayama, "Optical, structural and composition properties of silicon nitride films deposited by reactive radio-frequency sputtering, low pressure and plasma-enhanced chemical vapor deposition," *Thin Solid Films* p. 139568 (2022). URL <https://www.sciencedirect.com/science/article/pii/S0040609022004710>.
2. K. Luke, Y. Okawachi, M. R. E. Lamont, A. L. Gaeta, and M. Lipson, "Broadband mid-infrared frequency comb generation in a Si3N4 microresonator," *Opt. Lett.* **40**(21), 4823–4826 (2015). URL <https://opg.optica.org/ol/abstract.cfm?URI=ol-40-21-4823>.
3. W. D. Sacher, X. Luo, Y. Yang, F.-D. Chen, T. Lordello, J. C. C. Mak, X. Liu, T. Hu, T. Xue, P. G.-Q. Lo, M. L. Roukes, and J. K. S. Poon, "Visible-light silicon nitride waveguide devices and implantable neurophotonic probes on thinned 200 mm silicon wafers," *Opt. Express* **27**(26), 37,400–37,418 (2019). URL <https://opg.optica.org/oe/abstract.cfm?URI=oe-27-26-37400>.
4. G. N. West, W. Loh, D. Kharas, C. Sorace-Agaskar, K. K. Mehta, J. Sage, J. Chiaverini, and R. J. Ram, "Low-loss integrated photonics for the blue and ultraviolet regime," *APL Photonics* **4**(2), 026,101 (2019). <https://doi.org/10.1063/1.5052502>, URL <https://doi.org/10.1063/1.5052502>.
5. C. Sorace-Agaskar, D. Kharas, S. Yegnanarayanan, R. T. Maxson, G. N. West, W. Loh, S. Bramhavar, R. J. Ram, J. Chiaverini, J. Sage, and P. Juodawlkis, "Versatile Silicon Nitride and Alumina Integrated Photonic Platforms for the Ultraviolet to Short-Wave Infrared," *IEEE Journal of Selected Topics in Quantum Electronics* **25**(5), 1–15 (2019).
6. E. Shim, Y. Chen, S. Masmanidis, and M. Li, "Multisite silicon neural probes with integrated silicon nitride waveguides and gratings for optogenetic applications," *Scientific Reports* **6**(1), 22,693 (2016). URL <https://doi.org/10.1038/srep22693>.
7. J. A. Smith, H. Francis, G. Navickaite, and M. J. Strain, "SiN foundry platform for high performance visible light integrated photonics," *Opt. Mater. Express* **13**(2), 458–468 (2023). URL <https://opg.optica.org/ome/abstract.cfm?URI=ome-13-2-458>.
8. M. Gao, Q.-F. Yang, Q.-X. Ji, H. Wang, L. Wu, B. Shen, J. Liu, G. Huang, L. Chang, W. Xie, S.-P. Yu, S. B. Papp, J. E. Bowers, T. J. Kippenberg, and K. J. Vahala, "Probing material absorption and optical nonlinearity of integrated photonic materials," *Nature Communications* **13**(1), 3323 (2022). URL <https://doi.org/10.1038/s41467-022-30966-5>.
9. J. Liu, G. Huang, R. N. Wang, J. He, A. S. Raja, T. Liu, N. J. Engelsen, and T. J. Kippenberg, "High-yield, wafer-scale fabrication of ultralow-loss, dispersion-engineered silicon nitride photonic circuits," *Nature Communications* **12**(1), 2236 (2021). URL <https://doi.org/10.1038/s41467-021-21973-z>.
10. N. Chauhan, J. Wang, D. Bose, K. Liu, R. L. Compton, C. Fertig, C. W. Hoyt, and D. J. Blumenthal, "Ultra-low loss visible light waveguides for integrated atomic, molecular, and quantum photonics," *Opt. Express* **30**(5), 6960–6969 (2022). URL <https://opg.optica.org/oe/abstract.cfm?URI=oe-30-5-6960>.
11. M. H. P. Pfeiffer, J. Liu, A. S. Raja, T. Morais, B. Ghadiani, and T. J. Kippenberg, "Ultra-smooth silicon nitride waveguides based on the Damascene reflow process: fabrication and loss origins," *Optica* **5**(7), 884–892 (2018). URL <https://opg.optica.org/optica/abstract.cfm?URI=>

- [optica-5-7-884](#).
12. M. Borselli, T. J. Johnson, and O. Painter, "Beyond the Rayleigh scattering limit in high-Q silicon microdisks: theory and experiment," *Opt. Express* **13**(5), 1515–1530 (2005). URL <https://opg.optica.org/oe/abstract.cfm?URI=oe-13-5-1515>.
 13. C. Xiang, W. Jin, J. Guo, C. Williams, A. M. Netherton, L. Chang, P. A. Morton, and J. E. Bowers, "Effects of nonlinear loss in high-Q Si ring resonators for narrow-linewidth III-V/Si heterogeneously integrated tunable lasers," *Opt. Express* **28**(14), 19,926–19,936 (2020). URL <https://opg.optica.org/oe/abstract.cfm?URI=oe-28-14-19926>.
 14. M. W. Puckett, K. Liu, N. Chauhan, Q. Zhao, N. Jin, H. Cheng, J. Wu, R. O. Behunin, P. T. Rakich, K. D. Nelson, and D. J. Blumenthal, "422 Million intrinsic quality factor planar integrated all-waveguide resonator with sub-MHz linewidth," *Nature Communications* **12**(1), 934 (2021). URL <https://doi.org/10.1038/s41467-021-21205-4>.
 15. S. Kluska, M. Jurzecka-Szymacha, N. Nosidlak, P. Dulian, and J. Jaglarz, "The Optical and Thermo-Optical Properties of Non-Stoichiometric Silicon Nitride Layers Obtained by the PECVD Method with Varying Levels of Nitrogen Content," *Materials* **15**(6) (2022). URL <https://www.mdpi.com/1996-1944/15/6/2260>.
 16. A. W. Elshaari, I. E. Zadeh, K. D. Jöns, and V. Zwiller, "Thermo-Optic Characterization of Silicon Nitride Resonators for Cryogenic Photonic Circuits," *IEEE Photonics Journal* **8**(3), 1–9 (2016).
 17. J. G. E. Gardeniers, H. A. C. Tilmans, and C. C. G. Visser, "LPCVD silicon-rich silicon nitride films for applications in micromechanics, studied with statistical experimental design*," *Journal of Vacuum Science & Technology A* **14**(5), 2879–2892 (1996). <https://doi.org/10.1116/1.580239>, URL <https://doi.org/10.1116/1.580239>.
 18. H. Nejadriahi, A. Friedman, R. Sharma, S. Pappert, Y. Fainman, and P. Yu, "Thermo-optic properties of silicon-rich silicon nitride for on-chip applications," *Opt. Express* **28**(17), 24,951–24,960 (2020). URL <https://opg.optica.org/oe/abstract.cfm?URI=oe-28-17-24951>.
 19. N. G. Pruiti, C. Klitis, C. Gough, S. May, and M. Sorel, "Thermo-optic coefficient of PECVD silicon-rich silicon nitride," *Opt. Lett.* **45**(22), 6242–6245 (2020). URL <https://opg.optica.org/ol/abstract.cfm?URI=ol-45-22-6242>.
 20. M. Soltani, "Novel integrated silicon nanophotonic structures using ultra-high Q resonators," (2009). Publisher: Georgia Institute of Technology, URL <http://hdl.handle.net/1853/31647>.
 21. F. Ladouceur and L. Poladian, "Surface roughness and backscattering," *Opt. Lett.* **21**(22), 1833–1835 (1996). URL <https://opg.optica.org/ol/abstract.cfm?URI=ol-21-22-1833>.
 22. D. Melati, F. Morichetti, and A. Melloni, "A unified approach for radiative losses and backscattering in optical waveguides," *Journal of Optics* **16**(5), 055,502 (2014). URL <https://dx.doi.org/10.1088/2040-8978/16/5/055502>.
 23. G.-L. Tan, M. F. Lemon, and R. H. French, "Optical Properties and London Dispersion Forces of Amorphous Silica Determined by Vacuum Ultraviolet Spectroscopy and Spectroscopic Ellipsometry," *Journal of the American Ceramic Society* **86**(11), 1885–1892 (2003). <https://ceramics.onlinelibrary.wiley.com/doi/pdf/10.1111/j.1151-2916.2003.tb03577.x>, URL <https://ceramics.onlinelibrary.wiley.com/doi/abs/10.1111/j.1151-2916.2003.tb03577.x>.
 24. J. A. Guerra, A. Tejada, J. A. Töfflinger, R. Grieseler, and L. Korte, "Band-fluctuations model for the fundamental absorption of crystalline and amorphous semiconductors: a dimensionless joint density of states analysis," *Journal of Physics D: Applied Physics* **52**(10), 105,303 (2019). URL <https://dx.doi.org/10.1088/1361-6463/aaf963>.
 25. F. P. Payne and J. P. R. Lacey, "A theoretical analysis of scattering loss from planar optical waveguides," *Optical and Quantum Electronics* **26**(10), 977–986 (1994). URL <https://doi.org/10.1007/BF00708339>.
 26. J. Lacey and F. Payne, "Radiation loss from planar waveguides with random wall imperfections," *IEE Proceedings J (Optoelectronics)* **137**, 282–289(7) (1990). URL <https://digital-library.theiet.org/content/journals/10.1049/ip-j.1990.0047>.
 27. X. Ji, F. A. S. Barbosa, S. P. Roberts, A. Dutt, J. Cardenas, Y. Okawachi, A. Bryant, A. L. Gaeta, and M. Lipson, "Ultra-low-loss on-chip resonators with sub-milliwatt parametric oscillation threshold," *Optica* **4**(6), 619–624 (2017). URL <https://opg.optica.org/optica/abstract.cfm?URI=optica-4-6-619>.